GROUND BASED OBSERVATIONS

Optical and Infrared Imaging

Our campaign of optical and IR observations of GRB 090423 began roughly 40 seconds post burst, and continued for ~20 days. The facilities used in this campaign included the Burst Observer and Optical Transient Observing System (BOOTES-3) Yock-Allen telescope in New Zealand, the Palomar 60 inch[29], the 3.9m United Kingdom Infrared Telescope (UKIRT, equipped with the eStar system[30]), the Gemini North and South Observatories, the Russian 6.0m BTA, the Max-Planck-Institute/ESO 2.2m Telescope and GRB Optical and NIR Detector (GROND) 7-channel imager[31] and the European Southern Observatories (ESO) Very Large Telescope (VLT), Antu and Yepun (UT1 and UT4) units. Imaging observations have been reduced using the standard techniques. Aperture photometry has been performed, and results are given relative to the nearby bright star at RA=09:55:35.31, Dec =18:09:30.9, which has tabulated magnitudes of r=17.778(0.006), i=16.537(0.005), z=15.905(0.004), Y=15.25(0.02), J=14.523(0.031), H=13.972(0.036), K=13.773(0.049), (numbers in parenthesis correspond to 1-sigma errors). Optical magnitudes for this star are derived from Sloan Digital Sky Survey (SDSS) observations[32], while nIR measurements are obtained by the 2-Micron All Sky Survey (2MASS)[33]. Our Y-band measurements come from the field calibration of Im et al[34]. Colour terms for our different filters are minimal and are not considered. Upper limits are stated at 3-sigma confidence levels. In addition, the fluxes shown correspond to sky subtracted flux, measured in an aperture centred on the location of the afterglow. In observations where the afterglow is not visible its location has been derived by relative astrometry between filters where the object is bright, and those where it is undetected. Roughly 10 point sources common to each image were used for this alignment in the Image Reduction and Analysis Facility (IRAF) task *geomap*. The

resulting astrometric fits are better than 0.05 arcseconds (better for cases of aligning images taken with the same instrument). A mosaic, showing multicolour images of the GRB 090423 afterglow taken at three separate epochs is shown in Figure S01, while a full log of all photometric observations considered in this paper is included in Table S1.

Infrared Spectroscopy

Near-infrared spectroscopy was first obtained using the VLT Imaging Spectrometer and Array Camera (ISAAC). Data were obtained using the J grism (~1.08 - 1.32 micron; midpoint 17.94 hr after burst) for a total of 36 min exposure time, and in the SZ grism (~0.92 - 1.20 micron) for a total exposure time of 45 min. The data were acquired in a large (60") nodding pattern along the slit, with individual exposures of 60 s, to facilitate sky subtraction, while telluric standard stars were observed at similar airmass, immediately following the science observations. The data were processed using the ESO / ISAAC pipeline, which includes sky subtraction, flat fielding, wavelength calibration, spectral image registration and co-addition. Finally we rectified the spectra to produce horizontal traces, and removed a 50 Hz pickup pattern. The fully reduced science frame of the J-grism data shows a clear detection of the source, whereas no trace is visible in the reduced SZ-grism frame. The spectrum of the afterglow was obtained with the IRAF *apall* task, using the trace of the telluric standard as a reference aperture. Telluric correction and flux calibration was achieved using the IDL / SpeXtool package *xtellcor_general*[35], using a high quality Vega model convolved with known telluric absorption features to match the entire telluric standard (HD 58784, B3III) spectrum. This model is then applied to the science target spectrum, producing a telluric feature corrected and fully flux calibrated spectrum (excepting slit losses); the data are completely corrected for instrument sensitivity. A small (3 km/s) wavelength shift was applied to the telluric standard to minimize residual noise near significant

telluric features. The final flux calibration of the J-grism spectrum was achieved using the J-band photometry of the afterglow.

We obtained further near-infrared spectroscopy on the 24th April, using the VLT Spectrograph for Integral Field Observations in the Near Infrared (SINFONI). Data were obtained using the J grism, providing a spectral resolution of ~2000, using a 8" x 8" field of view. Fifteen exposures, each of 600 seconds were obtained, with midpoint 1.276 days after burst. We reduced the data using the ESO esorex SINFONI pipelines, version 1.9.4. This includes correction for detector signatures: bad pixels, detector contribution to the measured signal, dark current, flat fielding (correct pixel to pixel gain variations and relative slitlet throughput differences) and geometric distortions. Wavelength calibration was performed using arc spectra as well as OH sky lines. After these reductions, the image slices were combined using the spatial and spectral information to form a 3-dimensional datacube. In the co-added cube a source is visible when adding together all wavelength slices. We extracted a 1-dimensional spectrum of this source by using a 5 pixel radius Gaussian-weighted aperture at the source position. To correct for some residual sky emission lines and thermal signatures, we extracted sky spectra from the same cube (besides the afterglow no other sources are visible in the 8"x8" field of view), and subtracted this sky spectrum from the science spectrum. We reduced and extracted the spectrum of the telluric standard star (HD 88322, type B4V) in the same manner, using the same routines to correct for telluric transmission and flux calibrate as for the ISAAC spectroscopy. Though the signal-to-noise is low, the high resolution of the SINFONI spectroscopy offers larger windows between sky lines, and the final spectrum plotted (Figure S06) shows 100 Angstrom wide bins in which the flux in the target aperture has been coadded using variance-weighting to down-weight frames badly affected by high sky background.

Both ISAAC and SINFONI spectroscopy show clear breaks at around 1.13 microns. More detailed spectral fitting, and the constraints that this yields on the redshift are presented below. A log of the spectroscopic observations is shown in Table S2.

SWIFT OBSERVATIONS

The *Swift* Burst Alert Telescope (BAT) triggered on GRB 090423 at 07:55:19 UT on 23 April 2009, yielding a prompt position with a 3 arcminute error radius (90% confidence)[36]. Observations with the narrow field instruments (the X-ray Telescope (XRT) and UV and Optical Telescope (UVOT)) began approximately 70 seconds after the burst. Observations with the XRT ultimately yielded a position accurate to 1.7 arcseconds[37,38]. The UVOT observations yielded no detection as expected for a source at z~8 (ref 39). A summary of the results of the BAT and XRT observations is provided in Table S3, while more details are given in the next sections.

Properties of prompt emission

The prompt gamma-ray light-curve of GRB 090423 consists of two peaks with a total duration t_{90} of 10.3 ± 1.1 seconds, with a fluence of $5.9 \pm 0.4 \times 10^{-7}$ ergs cm^{-2} (15-150 keV). Its prompt spectrum can be fit with either a Band function[40] or a cut-off power-law, which yields a peak energy (E_p) of ~50 keV [ref 41,42]). In particular, comparing the properties of the prompt emission of GRB 090423 with those of lower-z GRBs shows no obvious differences that may be expected from time dilation or spectral softening as the harder photons are redshifted. Hence, in terms of these basic properties GRB 090423 is broadly consistent with the wider GRB population observed by *Swift*, and does not have obvious features that would allow it to be identified as a high-*z*

candidate based on prompt properties alone. Further, there is no requirement from these data for any progenitor (or afterglow) models which are distinct from those developed to explain other GRBs.

Our extraction of the BAT light-curve is shown in Figure 3 of the main text. The BAT light-curve was binned such that each point had a signal-to-noise ratio of at least 5. A BAT spectrum was extracted over the T90 interval and fitted with a cut-off power-law, which was found to have index 0.80. This model was extrapolated down to 0.3-10 keV, to estimate the flux over the XRT band. The ratio of this flux and the mean count rate of the spectrum gave the counts to flux conversion factor which was applied to the light-curve.

X-ray afterglow light-curve

Observations of GRB 090423 with the *Swift* X-ray telescope began 73 seconds post burst, and were obtained principally in photon counting mode. The X-ray light-curve is shown in Figure 3 of the main article, and is derived using the techniques of ref 43. Excluding the early flare, it can be fit by a broken power-law with a plateau followed by a steeper decay with indices of, $\alpha_{1,x} = -0.04^{+0.12}_{-2.46}$ and $\alpha_{2,x} = 1.40^{+0.08}_{-0.07}$, and a break time of $t_{b,x} = 5050^{+530}_{-4050}$ seconds (all errors at 90% confidence). A further description of the light-curve (which was created following ref 44), and its comparison with the optical/IR light-curve is provided below.

X-ray spectroscopy

The X-ray spectrum (created using the tools of ref 44**)** is adequately fit by a single power-law plus absorption due to both a fixed Galactic column and host galaxy contribution. Fitting to all the data yields $\Gamma = 1.76^{+0.09}_{-0.10}$, while ignoring the flare provides $\Gamma = 2.05^{+0.14}_{-0.09}$. Splitting the data in segments before the flare, in the plateau and in the late decay shows no strong evidence for spectral evolution, with the afterglow spectral slope consistent with Γ=2 (β= (Γ-1) ~ 1) in each of these segments. The

inclusion of the flare does result in an apparent hardening of the spectral slope, but this is not unusual in flares, and hence we will exclude the flare in subsequent analysis.

The best fitting excess column density is $N_{HI} = 1.16^{+0.50}_{-0.58} \times 10^{23}$ cm^{-2} at z=8.3, with the flare excluded, or $N_{HI} = 6.34^{+2.76}_{-2.92} \times 10^{22}$ cm^{-2} including the flare. These fits are reported as excess absorption, above the Galactic value, which was fixed in our fits at $N_{HI} = 2.89 \times 10^{20}$ cm^{-2} (ref 45). To investigate the nature of possible excess absorption in the X-ray afterglow of GRB 090423 we plot in Figure S02 the observed X-ray spectrum, fitted with our best fit model. In addition we also show the improvement in the residuals with the application of an additional absorber. Because the redshift of GRB 090423 is so large the soft X-rays, which are most readily attenuated, are largely redshifted out of the XRT band, and hence even the apparently small curvature would correspond to very large column densities in the rest frame of GRB 090423. Taken at face value this suggests a column ~1 × 10^{23} cm^{-2}, which would lie at the high end of observed values for *Swift* GRBs[46]. To investigate the necessity of excess absorption we investigate the goodness of fit over the photon index – N_{HI} parameter space. The results are also shown in Figure S02. Ultimately, the evidence for excess absorption appears relatively weak (~3 sigma), and may well have a rather lower value. Further, it is possible that any excess absorption could be due to additional absorption in any intervening systems at lower-z along the line of sight (again such systems are not uncommon in GRB afterglows[47]). Hence we do not consider that the apparent observation of excess absorption in GRB 090423 makes it exceptional.

Finally we note that there is very little correlation observed between the H I column inferred from X-ray absorption and that inferred from Lyman-alpha[46]. The X-ray absorption therefore has little implication for the expected host absorption in the NIR.

DATA ANALYSIS AND INTERPRETATION

NIR Light-curve evolution and comparison with X-rays

As with the X-ray light-curve the IR light-curve of GRB 090423 apparently shows some complexity, although the IR follow-up is relatively sparse in comparison to the X-ray. To improve the sampling we have extrapolated all of our optical/IR photometric points to a single photometric band (the J-band) using our best-fit spectral model. We then fit this combined light-curve, and compare the results to those obtained from the X-ray.

Both X-ray and IR exhibit a plateau phase, followed by a break to a steeper decay. Ignoring the final two IR points (see below) the decay indices in both plateau ($\alpha_{1,x} = -0.043^{+0.119}_{-2.46}, \alpha_{1,IR} = -0.01^{+0.028}_{-0.040}$) and later decay phases ($\alpha_{2,x} = 1.40^{+0.08}_{-0.07}, \alpha_{2,IR} = 1.36^{+0.33}_{-0.22}$) are consistent with each other within the fitted errors. However, the break time is apparently later in the IR than the X-ray ($t_{\mathrm{b},x} = 5050^{+530}_{-4050}$ s, $t_{\mathrm{b},IR} = 24200^{+9100}_{-4400}$ s).

At times >2 days there is an apparent flattening of the IR decay, which could also be interpreted as an optical flare. We have not included these data in the fit shown in Figure 3 of the main article. However, it is relevant to consider alternative interpretations here. Including the two data points which indicate a flare (J and K band observations taken on the night of 26 April) in the fit yields a shallower later time decay index $0.96^{+0.06}_{-0.08}$, and earlier break time $t_{\mathrm{b},IR} = 16300^{+2500}_{-1300}$ seconds, but a poor χ^2/dof (29.97/13=2.305, compared to 7.051/11=0.641 for the fit ignoring these points). Including these data by fitting two additional power-laws (one which accounts for the flattening, and another which requires a later break as implied by limits obtained roughly 7 and 15 days post burst) improves the χ^2/dof to (10.81/10=)1.081 but the probability of random improvement is non-trivial (1.4% using an F-test). A final possibility is that the mid-time IR observations are not representative of the IR decay, but themselves contain contamination in the form of an IR flare at ~60ks. In this case the break from the plateau occurs at $t_{\mathrm{b},IR} = 6740^{+2580}_{-540}$ s, which within the errors allows

the IR and X-ray breaks to be nearly simultaneous at ~6000s. This fit also produces a much shallower post-break decline with a late time slope of $\alpha_{2,IR} = 0.69^{+0.08}_{-0.04}$. However, in this case a further break would be required to accommodate the late time K-band upper limit.

Spectral energy distribution

The spectral energy distribution of the GRB 090423 afterglow, and its time evolution are shown in Figure S03. In the nIR it appears very blue, with a spectral slope of index $\beta = 0.26 \pm 0.10$ (based on the average spectral fit for our first three epochs of observations (UKIRT+Gemini-N, VLT+Gemini-S and GROND)**.** Although this is extremely blue, it is not unprecedented with some previous GRBs showing similar spectral slopes (e.g. GRB 021004[ref 48], GRB 080319B[ref 49]). There is little evidence for evolution over the time period of the observations. However, the final epoch of *J* and *K* and observations do show a redder colour than previous epochs ($(J-K)_{\rm early} = 1.34 \pm 0.05$ and $(J-K)_{\rm late} = 1.61 \pm 0.13$). Given the associated errors the evidence for reddening is marginal (~2 sigma) and we do not consider it compelling. Further, as noted above the light-curve of GRB 090423 shows evidence for a possible flare at the time of these final epoch observations, which may explain any observed colour difference.

We additionally investigated the joint X-ray – opt/IR spectral fit[50], which is also shown in Figure S03. Our early (1.5 hour) SED suggests best fit values of $\beta_x = 0.80^{+0.06}_{-0.05}$, with $\beta_{IR} = 0.30^{+0.06}_{-0.05}$ (with a fixed $\Delta\beta = 0.5$ for a cooling break), with a cooling break at $0.02^{+0.04}_{-0.01}$ keV, no host extinction is required, $A_V < 0.08$ (the overall χ^2/dof for this ft is 20.79/18 = 1.16). Should the X-ray and IR lie in different cooling regimes then the post-break decay slopes should be different by $\Delta\alpha = 0.25$, given the large errors on the

measurement of $\alpha_{2,IR}$, this is consistent with the observations. The late time fit, obtained at the time of the possible IR flare shows that the X-ray to optical spectral index has increased to $\beta_x = 0.90^{+0.10}_{-0.07}$, which is also consistent with the measured β_{IR} at the same epoch. However, this is likely to be due to the IR flare, rather than unusually rapid motion of the cooling break.

Photometric redshift

The strong break between the *Y* and *J* band provides compelling evidence for the high redshift origin of GRB 090423. However, to formalize the constraints that can be obtained from the photometric observations we performed a photometric redshift fit to the available photometry. We normalized the observations to a common epoch, allowing for the fading afterglow as described in the light-curve section. We chose an epoch centred at the time of the Gemini-South, VLT and GROND observations, and fit the resulting photometry in the standard *hyperz* photometric redshift code[51], on the assumption that the underlying spectrum would be well described as a power-law. At this point we also corrected our photometry for the small foreground extinction of E(*B*-*V*) = 0.029 and accounted for the differing filter response functions. In particular, the GROND *J*-band filter extends to ~1.1 microns, while the HAWK-I *J* has little transmission below ~1.16 microns. Hence the GROND J-band photometry will encompass Lyman-alpha for any z>8.04

The resulting photometric redshift fit is shown in Figure S04, and is $z = 8.06^{+0.21}_{-0.28}$, which is in excellent agreement with results obtained via direct spectroscopy. There is no requirement for any host galaxy dust extinction within the fit. We further note that this approach does not include a detailed modelling of the damping wing from either the intergalactic medium (IGM) or a host Lyman-alpha absorption, both of which would tend to deplete the blue flux around the break. The impact of including such extra parameters is relatively small (typically of order 1% in the photo-z), but would favour a

somewhat higher redshift, with larger associated errors. This effect is considered in greater detail in the spectral fitting described below.

Spectroscopic constraints on the redshift of GRB 090423

The 1D spectra shown in Figure 2 of the main article were created by taking the fluxed and calibrated 1D spectra and binning the channels together using error weighting. The bin sizes were adjusted so that the final uncertainty on the flux in each bin was approximately the same, around 6 μJy. This can clearly be seen, with much larger bins in the parts of the spectrum with greater sky noise or lower throughput. The 2D spectra shown in that Figure were also binned into larger pixels using error weighting, but in this case the pixel size was kept constant, and the final spectra Gaussian smoothed to help visualisation. The relative throughput for the two ISAAC spectra as a function of wavelength is shown in Figure S05.

Ideally, a firm redshift could be obtained by the location of narrow absorption lines in the afterglow spectrum. However, none were obviously visible in the data, due in part to the low signal to noise ratio. To provide a more robust search for spectral features we co-added regions of the spectrum which would contain strong absorption lines, similar to those seen in the afterglow of GRB 050904 (ref 52). Namely the lines of SiII, CIV and OI. We then stepped through the spectrum fitting all redshifts for $8.0 < z < 8.4$ to look for any dips which would represent the presence of these co-added absorption lines. However, no statistically significant dips were found, and hence we conclude that we cannot confidently derive a line redshift from the afterglow of GRB 090423.

Although a line redshift was not possible, the strong presence of a photometric break and two independent detections of a spectroscopic break via our ISAAC and SINFONI observations (Figure 2 in the main text and Figure S06) clearly demonstrate the presence of a strong spectral break in the afterglow spectrum of GRB 090423. Having ascertained the presence of the break it is important to consider the constraints that this places on the redshift. At first sight the presence of the break at ~11400 Angstroms equates directly to a redshift of about 8.4. However, the break is not necessarily so sharp, and we cannot make firm statements about its morphology directly from our low

signal to noise data. In particular, it is likely that the damping wing of Lyman-alpha is impacted by contributions from both the IGM[53] and the GRB host galaxy. Since GRB hosts frequently show strong Lyman-α absorption, a column of ~$10^{18\text{-}23}$ cm^{-2} could reasonably be expected[54], although the properties of any environments at z~8 are so unknown that such statements are inevitably speculative.

We fitted models to the Lyman-α damping wing based on those described in Barkana and Loeb[37]. Fitting was performed using χ^2 minimization. In this we allow both the redshift and neutral hydrogen column density in the host to be free parameters. In the fit shown in the main paper we set the neutral fraction in the IGM to be 10%, although the conclusions are fairly insensitive to this assumption, and fixed the slope and normalization of the power-law to that determined by the imaging photometry. To determine a confidence interval on the redshift determination, we conservatively assumed a flat prior on log(N_{HI}) between 19 and 23, and marginalised over that parameter. Higher log(N_{HI}) will deplete the blue flux, and tend to decrease the redshift measurement, lower values result in a sharper break, and a lower-z. A flat distribution is broadly consistent with the observed distribution of log(N_{HI}) values: arguably the true distribution is somewhat peaked around 21-21.5, and starting with a prior of that sort would have narrowed the error bars somewhat on the best-fit redshift. The final error bar is somewhat asymmetric, as expected since the upper limit on the redshift is rather hard, whereas very high values for log(N_{HI}) give increasingly lower values for the redshift due to the large breadth of the inferred damping wing. The best constraint on the redshift of GRB 090423 available from the ISAAC data is $z = 8.19^{+0.03}_{-0.06}$. The SINFONI spectrum (Figure S06), analysed in the same way, gives $z = 8.33^{+0.06}_{-0.11}$. These results are consistent with each other and, since they are arrived at independently, this gives considerable confidence in the robustness of the final result and also of the error estimates.

Combining the spectroscopy and photometry in a single analysis yields $z = 8.23^{+0.06}_{-0.07}$, which we regard as our most robust estimate of the redshift of GRB 090423. To illustrate the insensitivity of the redshift to assumptions about the state of the IGM ionization, if we take a 100% neutral fraction we find $z = 8.20^{+0.04}_{-0.03}$.

Time of obs (UT)	ΔT(s)	Telescope	Inst	Filter	Exp (s)	Magnitude	Flux (μJy)
23 April 07:55:59	40	BOOTES-3	-	Clear	2	>14.5	<4570
23 April 07:59:37	300	BOOTES-3	-	Clear	84	>18.5	<115
23 April 07:58:37	228	P60	-	r'	60	>21.9	<6.4
23 April 08:00:56	427	P60	-	r'	180	>22.3	<4.2
23 April 08:09:57	1268	P60	-	r'	780	>22.6	<3.3
23 April 08:00:02	313	P60	-	i'	60	>21.4	<9.6
23 April 08:08:19	930	P60	-	i'	300	>22.1	<5.1
23 April 08:14:46	1497	P60	-	i'	660	>22.6	<3.4
23 April 08:01:09	399	P60	-	z'	60	>19.8	<41.7
23 April 08:09:35	1016	P60	-	z'	300	>20.5	<23.3
23 April 08:16:34	1605	P60	-	z'	660	>21.1	<13.6
23 April 08:10:52	963	FTS	-	i'	60	>18.0	<230
23 April 08:15:37	1278	FTS	-	r'	120	>20.0	<36
23 April 08:18:36	1457	FTS	-	i'	120	>19.0	<91
23 April 08:25:18	1889	FTS	-	r'	180	>21.0	<14
23 April 08:29:18	2129	FTS	-	i'	180	>20.7	<19
23 April 08:16:32	1492	UKIRT	WFCAM	K	360	17.96 ± 0.04	40.1 ± 1.6
23 April 08:23:51	1961	UKIRT	WFCAM	K	360	17.94 ± 0.04	40.9 ± 1.6
23 April 08:32:09	2431	UKIRT	WFCAM	K	360	18.01 ± 0.04	38.3 ± 1.6
23 April 09:11:06	4780	Gemini-N	NIRI	Y	480	>22.5	0.27 ± 0.70
23 April 09:25:03	5560	Gemini-N	NIRI	J	480	19.24 ± 0.03	33.70 ± 1.01
23 April 09:39:27	6520	Gemini-N	NIRI	H	480	18.57 ± 0.02	36.60 ± 0.77
23 April 17:33:35	37790	6.0m BTA	SCORPIO	Ic	3600	>24.7	<0.29
23 April 23:08:00	60120	ESO2.2m	GROND	g	4000	>25.0	<0.36
23 April 23:08:00	60120	ESO2.2m	GROND	r	4000	>25.1	<0.33
23 April 23:08:00	60120	ESO2.2m	GROND	i	4000	>24.2	<0.76
23 April 23:08:00	60120	ESO2.2m	GROND	z	4000	>24.0	<0.91
23 April 23:08:00	60120	ESO2.2m	GROND	J	4000	20.66 ± 0.08	9.11 ± 0.55
23 April 23:08:00	60120	ESO2.2m	GROND	H	4000	19.94± 0.08	10.40 ± 0.83
23 April 23:08:00	60120	ESO2.2m	GROND	K	4000	19.36 ± 0.12	11.20 ± 1.22
23 April 23:38:21	58566	Gemini-S	GMOS	z	3000	>26.1	-0.005 ± 0.043
23 April 23:28:41	57860	VLT-UT4	HAWKI	K	2640	19.18 ± 0.03	13.20 ± 0.40
24 April 00:31:36	60620	VLT-UT4	HAWKI	J	1200	20.52 ± 0.04	10.40 ± 0.42
24 April 01:00:30	63250	VLT-UT4	HAWKI	Y	2640	>25.0	-0.08 ± 0.09
24 April 01:38:52	67440	ESO2.2m	GROND	J	4000	20.76 ± 0.07	8.31 ± 0.58
24 April 01:38:52	67440	ESO2.2m	GROND	H	4000	20.00 ± 0.07	9.81 ± 0.69
24 April 01:38:52	67440	ESO2.2m	GROND	K	4000	>19.8	<7.37
24 April 05:30:34	79695	UKIRT	WFCAM	K	3600	19.95 ± 0.14	6.49 ± 0.91

Time of obs (UT)	ΔT(s)	Telescope	Inst	Filter	Exp (s)	Magnitude	Flux (μJy)
24 April 23:36:36	144060	VLT-UT1	ISAAC	J	3600	21.80 ± 0.18	3.19 ± 0.51
27 April 01:04:05	321760	VLT-UT4	HAWKI	J	1200	22.19 ± 0.11	2.44 ± 0.27
27 April 00:01:14	318700	VLT -UT4	HAWKI	K	2640	20.58 ± 0.06	3.63 ± 0.22
30 April 23:06:33	661080	VLT-UT4	HAWKI	J	2400	>22.9	0.44 ± 0.24
8 May 23:29:09	1353510	VLT-UT4	HAWKI	K	2640	>21.8	0.22 ± 0.33

Table S1: Photometric observations of the GRB 090423 afterglow. The UT date refers to the start time of the observations, ΔT, is the mid-point of the observations, measured after the trigger time, which is 23 April 2009, 07:55:19.3 UT. The exposure time refers to the total on-source observation time. Magnitudes have not been corrected for the small foreground extinction of E(B-V) = 0.029. Errors are 1-sigma, and are statistical only.

Telescope	Instrument	λ-range (μm)	Time (UT)	ΔT (s)	Exp(s)	Resolution
VLT Antu (UT1)	ISAAC(SJ)	1.10-1.40	24 Apr 01:30:55	63335	2160	550
VLT Antu (UT1)	ISAAC(SZ)	0.98-1.10	24 Apr 02:35:24	67205	2700	500
VLT Yepun(UT4)	SINFONI(J)	1.10-1.40	24 Apr 23:12:21	141422	9000	2000

Table S2: Log of spectroscopic observations of the GRB 090423 afterglow. The wavelength range of each spectrum is shown, along with its start time and resolution. ΔT refers to the time since burst at the start of the observations

Fluence (15-150 keV)	$(5.9 \pm 0.4) \times 10^{-7}$ ergs cm^{-2}	
Peak Energy (E_p)	82 ±15 keV (Fermi) 48.6 ± 6.2 (BAT)	Von Kienlin GCN 9229
Rest frame peak energy	754 ± 138 keV (Fermi) 451 ± 58 (BAT)	
Isotropic equivalent energy (E_{ISO})	$(1.0 \pm 0.3) \times 10^{53}$ ergs (8-1000 keV)	Von Kienlin GCN 9229, 9251
X-ray afterglow photon index	$2.05^{+0.14}_{-0.089}$	
X-ray flux at 10 hours (0.3-10 keV) **X-ray flux at 10 hours restframe**	2.0×10^{-13} ergs s^{-1} cm^{-2} 2.5×10^{-14} ergs s^{-1} cm^{-2}	
X-ray luminosity at 10 hours (restframe)	2.1×10^{46} ergs s^{-1}	

Table S3: Basic prompt and afterglow properties of GRB 090423 as derived from the *Swift* BAT and XRT data, and our later time optical/IR observations. Additional parameters from the Fermi GBM have also been reported.

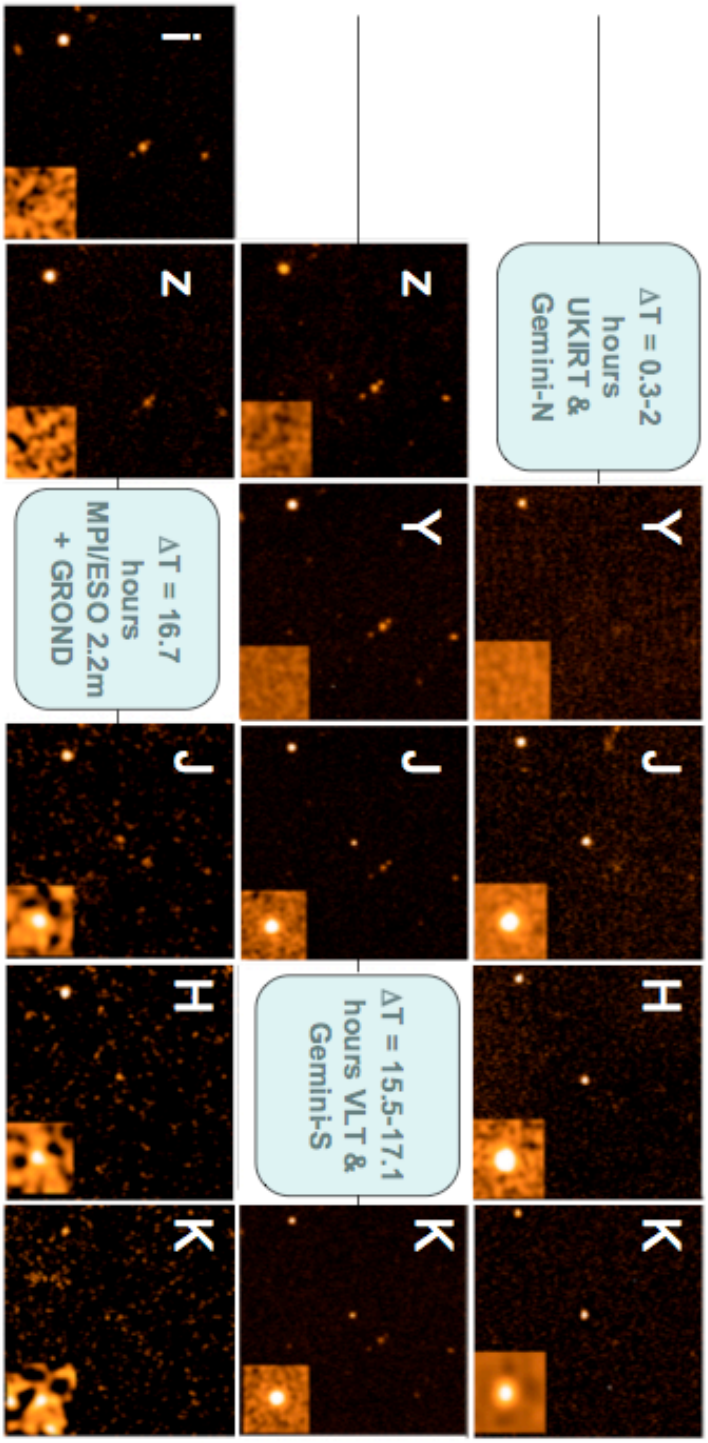

Figure S01: Mosaic showing multi-colour images of GRB 090423 obtained by UKIRT, Gemini-N, Gemini-S, the VLT and the MPI/ESO 2.2m over the first 24 hours post burst. All the data are consistent in showing a strong break between the Y and J-bands, and allow us to determine a photometric redshift of $z = 8.06^{+0.21}_{-0.28}$.

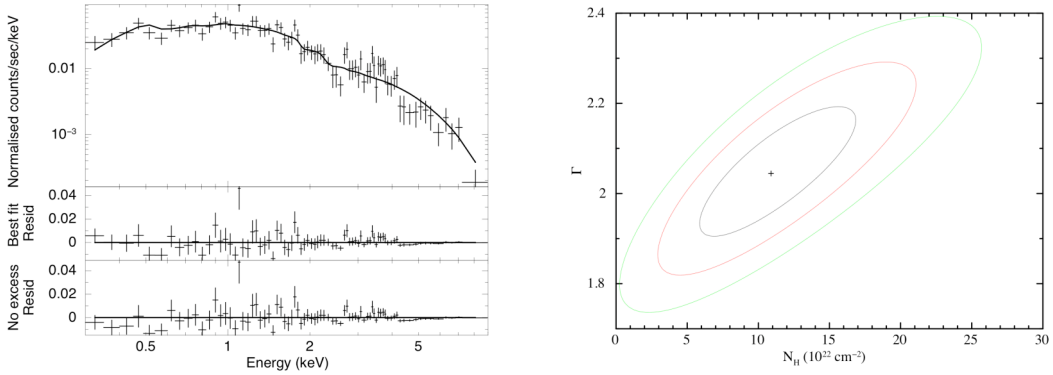

Figure S02: *Left:* The X-ray spectrum of GRB 090423 as observed by the *Swift* XRT. The two lower panels show the residuals to the best fit (which is shown as a solid line in the upper panel) and a fit in which zero additional extinction is included (bottom panel). This fit over-predicts the observed flux at low energies and suggests that excess column density is needed, which provides a slight improvement in the fit quality (middle panel). *Right:* Confidence contours in the N_H – photon index plane for the X-ray afterglow of GRB 090423. The contours represent 1, 2 and 3 sigma confidence levels. As can be seen, allowing for a varying photon index the column is consistent with zero at ~3 sigma. This suggests that the evidence for very strong X-ray absorption is relatively weak.

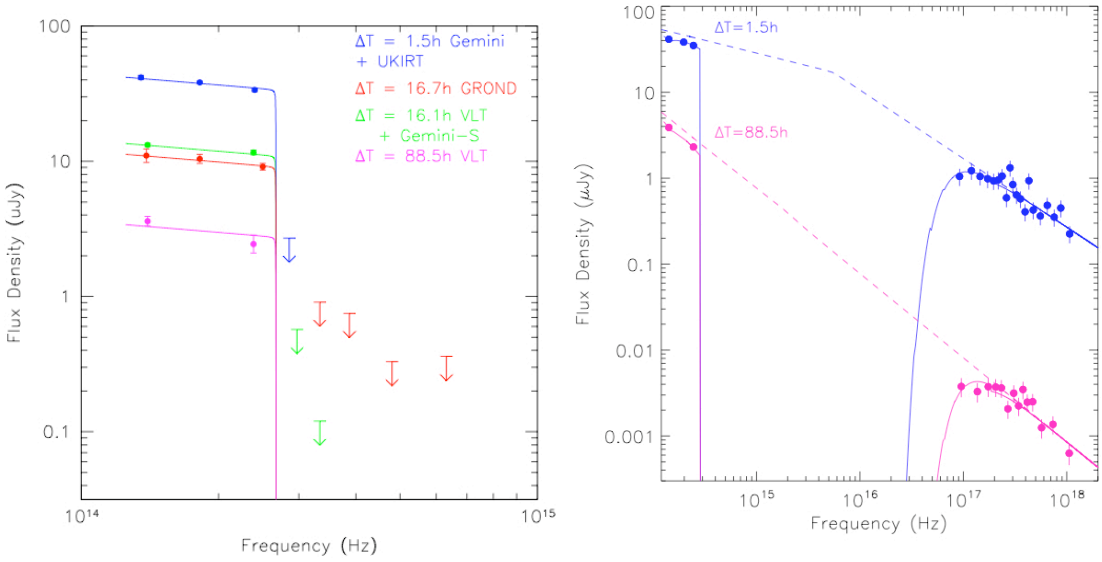

Figure S03: The spectral energy distribution of GRB 090423 measured at different times by our observations. The left hand panel shows only the optical/IR SED, plotted as frequency against flux density (F_ν). The observations are plotted, as are the limits at the 3-sigma level, for each epoch. Our strongest constraint on the observed SED comes from our VLT observations taken ~16.1 hours after the burst. In addition we have also plotted a model for the GRB afterglow, which has β=0.26, and a redshift of z=8.23. The right hand panel shows the optical to X-ray SED at two snapshots, 1.5 and 90 hours post burst. This implies the cooling break lies between the X-ray and the optical. The late time SED is likely impacted by the presence of a flare in the IR rather than unexpectedly rapid motion of the cooling break.

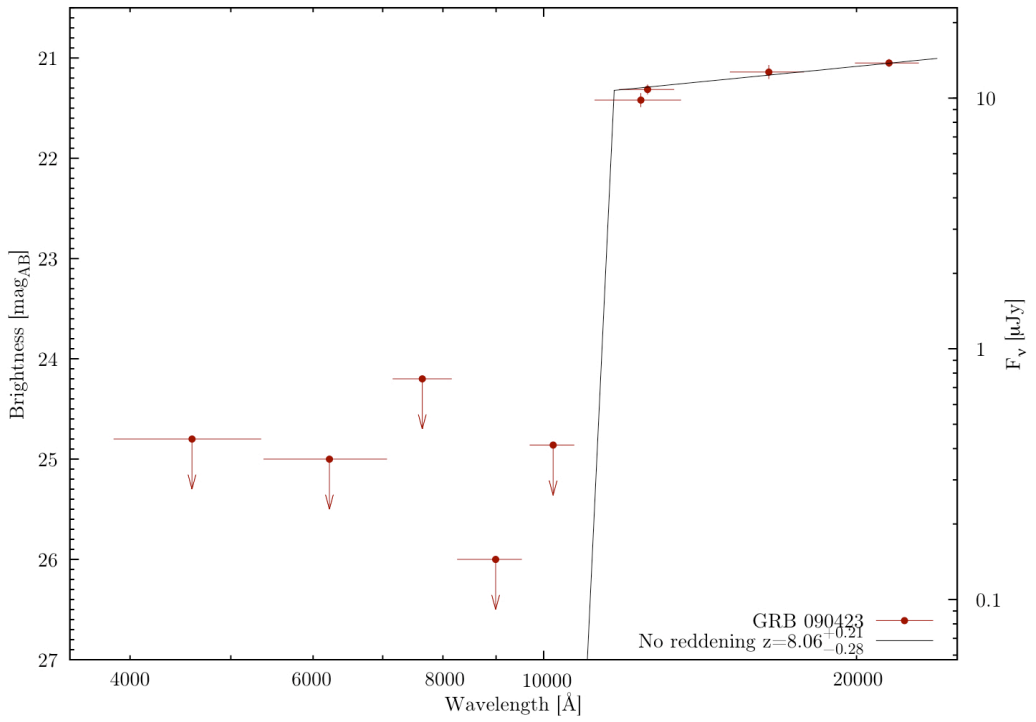

Figure S04: A photometric redshift fit for the afterglow of GRB 090423. The SED has been constructed at time t=16 hours, and makes use of constraints obtained from GROND, Gemini South Multi-Object Spectrograph (GMOS-S) and VLT High Acuity Wide field K-band Imager (HAWKI). The photo-z is found to be $z = 8.06^{+0.21}_{-0.28}$ in good agreement with the values obtained via spectroscopy.

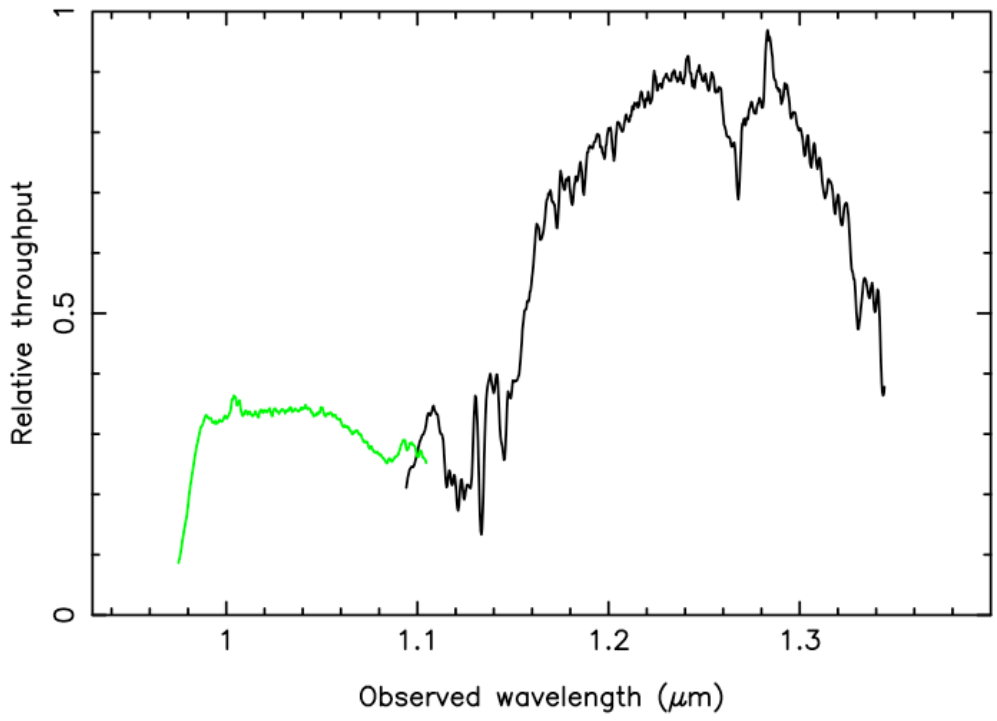

Figure S05: The relative throughput of the two ISAAC spectra (SZ in green and J in black) as determined by measurements of the telluric standard stars observed at similar air-mass and location as the science observations.

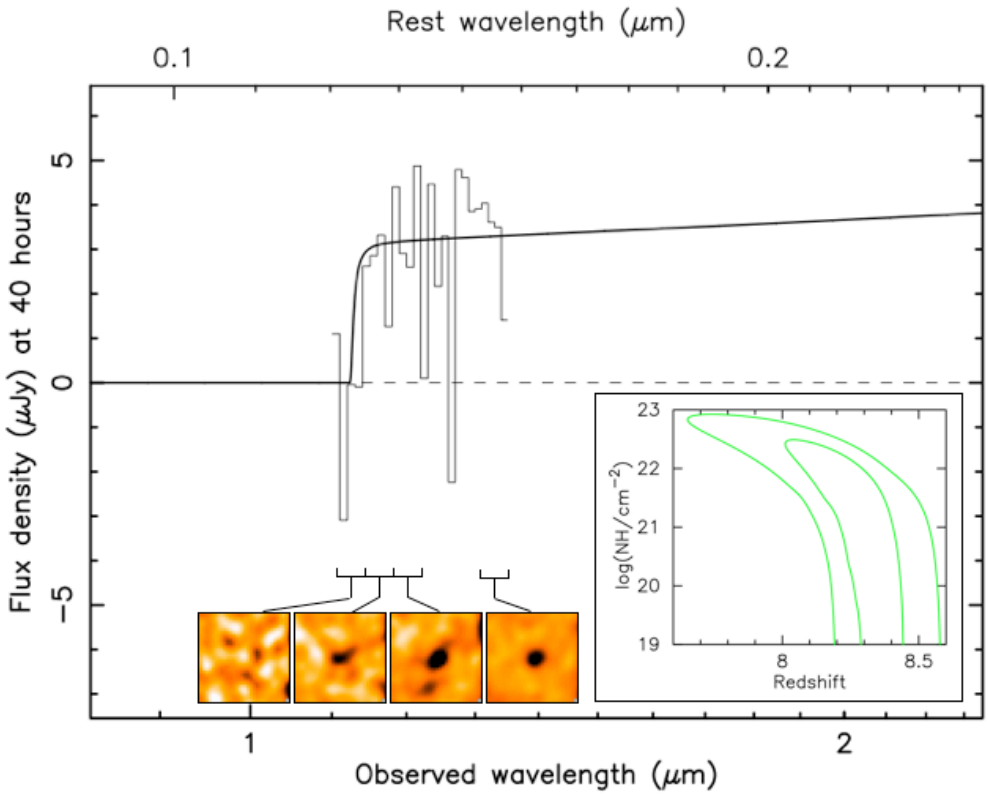

Figure S06: Our SINFONI IFU spectroscopy observations of GRB 090423, set on the same wavelength scale, and with the same overplotted model (renomalised), as Figure 2 from the main journal text for ease of comparison. The data were reduced as described in the text. The spectral bins are 100 Angstrom wide, and the images show individual 400 Angstrom wide sections of the data-cube that have been co-added (we avoid the regions worst affected by high sky noise). The afterglow is clearly visible long-ward of ~1.13 microns, but shows no evidence of detection short-ward of this value. As for Figure 2, the 68% and 95% confidence contours are shown, and provide excellent agreement with the redshift determined from our ISAAC spectroscopy, and an independent confirmation of this value.

SUPPLEMENTAL MATERIAL : REFERENCES

29. Cenko, S.B. et al. The Automated Palomar 60 Inch Telescope *Publications of the Astronomical Society of the Pacific* **118** 1396-1406 (2006)

30. Allan, A., Naylor, T. & Saunders, E. S. The eSTAR network - agent architectures for astronomy, *Astronomische Nachrichten*, **327** 767-770 (2006)

31. Greiner, J. *et al*. GROND – a 7 channel Imager, *Publications of the Astronomical Society of the Pacific* **120** 405-424 (2008)

32. Abazajian, K. *et al.* The Seventh Data Release of the Sloan Digital Sky Survey *Astrophys J. Supplement* **182** 543-558 (2008)

33. Skrutskie, M.F. *et al.* The Two Micron All Sky Survey (2MASS) *Astronomical Journal* **131** 1163-1183 (2006)

34. Im, M. et al. GRB 090423: Y-band field calibration update/correction, *GCN Circ* **9242**

35. Cushing, M.C., Vacca, M.D., & Rayner, J.T., Spextool: A Spectral Extraction Package for SpeX, a 0.8-5.5 micron Cross-Dispersed Spectrograph, *Publications of the Astronomical Society of the Pacific*, **116** 362-376 (2004)

36. Krimm, H. et al, GRB 090423: Swift detection of a burst *GCN Circ* **9198**

37. Stratta, G., Perri, M., GRB 090423: Swift-XRT refined analysis *GCN Circ* **9212**

38. Evans, P.A. et al. GRB 090423: Enhanced Swift-XRT position *GCN Circ* **9205**

39. De Pasquale, M., Krimm, H., GRB090423 - Swift/UVOT upper limits **9210**

40. Band, D. et al. BATSE observations of gamma-ray burst spectra: I – Spectra diversity, *Astrophys J.* **413** 281-292 (1993)

41. Palmer, D.M. et al. GRB 090423: Swift-BAT refined analysis, *GCN Circ* **9204**

42. Von Kienlin, A. GRB 090423: Fermi GBM observation , *GCN Circ* **9229**

43. Willingale, R. *et al.* Testing the Standard Fireball Model of Gamma-Ray Bursts Using Late X-Ray Afterglows Measured by Swift. *Astrophys. J.* **662**, 1093–1110 (2007).

44. Evans, P. *et al.* Methods and results of an automatic analysis of a complete sample of Swift XRT observations of GRBs.

45. Kalberla, P.M.W, Dedes, L. Global properties of the H I distribution in the outer Milky Way. Planar and extra-planar gas *Astronomy and Astrophysics* **487** 951-963 (2008)

46. Watson, D. et al. Very Different X-ray to Optical Column Density Ratios in gamma-ray burst Afterglows: Ionisation in GRB environments, *Astrophys J. Letters* **660** 101-104 (2007)

47. Prochter, G. et al. On the Incidence of Strong MgII Absorbers along Gamma-Ray Burst Sight Lines, *Astrophys J.* **648** L93-96 (2006)

48. Fynbo, J.P.U. et al. On the Afterglow and Host Galaxy of GRB 021004: A Comprehensive Study with the Hubble Space Telescope, *Astrophys J.* **633** 317-327 (2005)

49. Bloom, J. S. *et al.* Observations of the Naked-Eye GRB080319B: Implications of Nature's Brightest Explosion. *Astrophys. J.***691**, 723–737 (2009).

50. Schady, P. *et al.* Dust and gas in the local environments of gamma-ray bursts *Mon. Not. R. Astron. Soc.* **377** 273-284 (2007)

51. Bolzonella, M., Miralles, J-M., Pello, R. Photometric redshifts based on standard SED fitting procedures, *Astronomy & Astrophysics* **363** 476-492 (2000)

52. Kawai, N. et al. An optical spectrum of the afterglow of a gamma-ray burst at a redshift of 6.295, *Nature* **440** 184-186 (2006)

53. Barkana, R. & Loeb, A. Gamma-Ray Bursts versus Quasars: Lyα Signatures of Reionization versus Cosmological Infall, *Astrophys. J.* **601**, 64–77 (2004).

54. Jakobsson, P. et al. HI column densities of z>2 Swift gamma-ray bursts, *Astronomy and Astrophysics* **460** L13-17 (2006)